Hydrogen-anion-induced carrier recombination in $MAPbI_3$ perovskite solar cells

Yuhang Liang[1], Xiangyuan Cui[2,], Feng Li[1], Catherine Stampfl[1], Jun Huang[3], Simon P. Ringer[2], Rongkun Zheng[1,]**

Yuhang Liang, Dr. Xiangyuan Cui, Dr. Feng Li, Prof. Catherine Stampfl, Prof. Jun Huang, Prof. Simon P. Ringer, Prof. Rongkun Zheng

[1] School of Physics, The University of Sydney, NSW 2006, Australia

[2] School of Aerospace, Mechanical and Mechatronic Engineering, The University of Sydney, NSW 2006, Australia

[3] School of Chemical and Biomolecular Engineering, The University of Sydney, NSW 2006, Australia

*Email: carl.cui@sydney.edu.au, rongkun.zheng@sydney.edu.au

Keywords: perovskite solar cell, hydrogen interstitials, charge carrier recombination center, defect passivation, density functional theory

Abstract

Identification and passivation of defect-induced electron-hole recombination centers are currently crucial for improving the efficiency of hybrid perovskite solar cells. Besides general intrinsic defects, experimental reports have indicated that hydrogen interstitials are also abundant in hybrid perovskite layers; however, few reports have evaluated the effect of such defects on the charged recombination and device efficiencies. Here, we reveal that under I-poor synthesis conditions, the negatively charged monoatomic hydrogen interstitial, H_i^-, will form in the prototypical $CH_3NH_3PbI_3$ perovskite layer, acting as a detrimental deep-level defect, which leads to efficient electron-hole recombination and lowers the cell performance. We further rationalize that Br doping can mitigate the large atomic displacement caused by the presence of H_i^-, and hence suppress the formation of the deep localized state. The results advance the knowledge of the deep-level defects in hybrid perovskites and provide useful information for enhancing solar cell performance by defect engineering.

Introduction

Hybrid organic-inorganic perovskites have attracted significant interest as photovoltaic[1–3], and photoluminescent[4,5] technologies are based upon their unique and outstanding electrical and optical characteristics, such as long diffusion length[6,7] and strong light absorption[8]. In particular, hybrid perovskite solar cells have experienced an extraordinary increase in performance with the power conversion efficiency (PCE) skyrocketing from 3.8%[9] to recent 25.5%[10] over the past decade, already comparable with the best thin-film silicon solar cells.

Defect-induced charge carrier electron-hole recombination is a key factor underpinning the limitations in perovskite photovoltaic operation and affects further progress towards reaching the highest possible PCE defined by their thermodynamic limit[11–13]. Therefore, comprehensive identification and delicate passivation of deep-level defects are vital for further enhancing the PCE of perovskite solar cells. It is well established that the growth details of the perovskite layers are crucial for solar cell performance[11]. Higher cell efficiencies can be realized by the careful introduction of additional iodide ions; in contrast, synthesizing the materials with scarce iodine results in inferior performance. On the other hand, the highest PCE perovskite solar cells so far are essentially based on mixed halide (I & Br) perovskites[8,11,14–16]. In principle, the PCE of the prototypical $MAPbI_3$ ($MA= CH_3NH_3$) perovskite should reduce upon bromine doping because of the increased bandgap, based on the Shockley–Queisser limit[17]. But this contradicts the experimental finding: an abnormal increase of the PCE after Br doping was reported[14]. A general explanation is the defect-passivation of Br atoms[16]; however, the exact underlying mechanism, such as the passivating of which defects, and which deep levels, remains poorly understood.

Significant efforts[11,18–20] have been devoted to study intrinsic point defects to reveal the possible origin of deep-level nature in the prototypical hybrid perovskite $MAPbI_3$. The contribution of the charge carrier recombination losses has to date been assigned to intrinsic iodine interstitials (I_i)[21,22] and hydrogen vacancies from the host nitrogen atom ($V_{H(N)}^{-}$)[23]. Recently, experimental work has provided evidence that hydrogen is abundant in hybrid perovskites. While most studies reported positively charged hydrogen (H_i^+)[24–29], the negatively charged hydrogen was observed when synthesizing the perovskite with scarce iodine sources[30]. Besides the extrinsic introduction, e.g., the

growth precursors[7], the organic functional additives[25], the organic transporting layers[31], or the moisture ambient[24], the deprotonation of the organic cation of hybrid perovskite materials, e.g. $CH_3NH_3 \rightarrow CH_3NH_2 + H$ and $CH_3NH_3 \rightarrow CH_2NH_3 + H$, serves as a significant intrinsic hydrogen source for triggering defect formation. Delugas et al. have reported the latter process is energetically more favorable compaed with the former one, and the detached H tends to migrate toward PbI_6 octahedron and binds to an I anion[32]. The deprotonated methylamine (CH_3NH_2) molecule is stable and hence remains in a substitutional position at the A site[32]. Experiments indicaties that the intrinsic densities of the free hydrogen interstitial and deprotonated CH_3NH_2 are expected to be $\sim 10^{11} cm^{-3}$ in $MAPbI_3$ without any external stimulus[29]. This indicates that the "omnipresent" hydrogen interstitials could be incorporated in the perovskite layer even under encapsulation of photovoltaic cells or operation in the vacuum chamber. Moreover, the recently proposed hydrogen-rich growth conditions are essential to eliminate the detrimental intrinsic hydrogen vacancies for enabling the best solar cell performances[23]. Such growth conditions will in turn aggravate the unintentional introduction of hydrogen impurities. A big question, therefore, arises: whether the hydrogen interstitials have a profound impact on the performance of the perovskite solar cells? Our previous study theoretically confirmed the thermodynamic stability of hydrogen interstitials in perovskites[33]. However, the effects of such defects on the perovskite efficiencies especially their contributions to defect-induced charge carrier recombination processes have not been clarified.

In this paper, by performing first-principles density functional theory calculation, we theoretically revealed that in contrast to the shallow donor of H_i^+, the formation of H_i^- results in a large atomic displacement around the defect site, and creates a deep localized state in the bandgap, which serves as an exceptionally efficient nonradiative recombination channel and reduces the perovskite solar cell efficiencies. This gives a microscopic explanation for the inferior performance of the perovskites synthesized under iodine-poor conditions. We further rationalize that Br doping can effectively eliminate such a detrimental deep state.

Results and Discussions

Figure 1a shows the thermodynamic stable region for equilibrium growth of $MAPbI_3$

with respect to its pure elemental phases of constituent elements and competing secondary phases, i.e., MAI and PbI_2. Note the chemical potential for the desired $MAPbI_3$ perovskite is constrained in a narrow but long region, due to the small formation enthalpy of $MAPbI_3$ from MAI and PbI_2, indicative of the strict control for forming the stoichiometric $MAPbI_3$ perovskite layer. On the other hand, the flexible growth conditions, i.e., the flexibility available for the constituent compositional elements in precursors, can be chosen for tuning the material properties. Three representative points of chemical potential chosen, i.e., A, B, and C, which correspond to the perovskite growth conditions of I-rich/Pb-poor, moderate, and I-poor/Pb-rich, respectively.

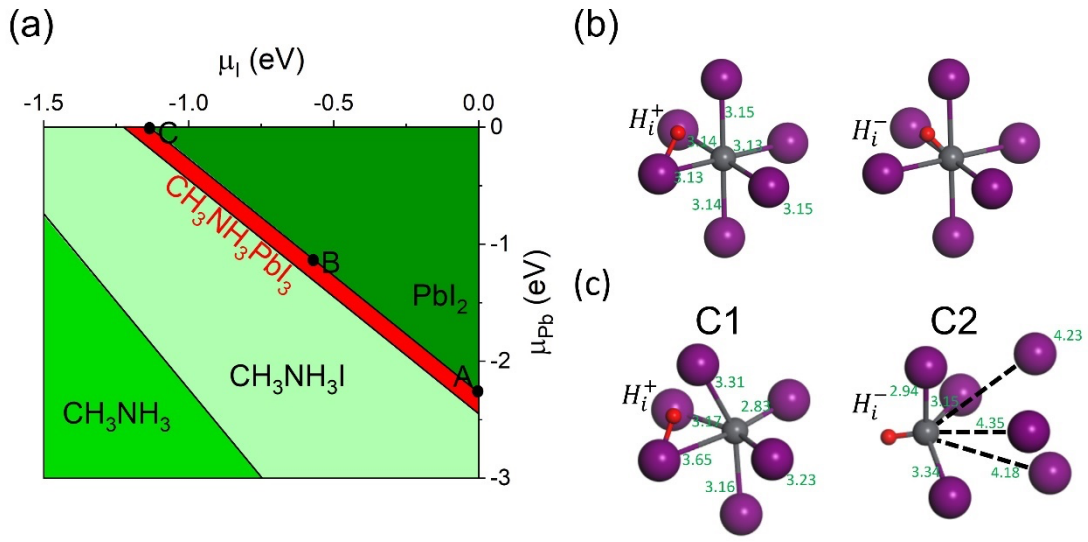

Figure 1. (a) The thermodynamically stable range for equilibrium growth of $MAPbI_3$ is a narrow, but long region colored by red. The local atomic structure of H_i^+ and H_i^- in $MAPbI_3$ (b) before and (c) after relaxation (MA not shown), in which the green numbers indicate the bond lengths or distances for the black dashed lines of the broken bonds. I atoms are depicted as purple spheres, Pb in grey, and the hydrogen impurities in red.

We have previously investigated the thermodynamic stability of hydrogen interstitials and found that both atomic and molecular hydrogen species can likely form in $MAPbI_3$ perovskite lattice[33], as shown in **Figure 2**. We also calculated the formation energies of four major intrinsic defects including two dominant donor defects, i.e., V_I^+ and Pb_i^{2+},

and two dominant acceptor defects, i.e., V_{Pb}^{2-} and V_{MA}^{-}, respectively, that are energetically most favorable in $MAPbI_3$ at the three different growth conditions. The results are consistent with the previous DFT studies[19,23,34], with some minor numerical differences due to the inclusion of the higher accuracy of HSE+SOC and dispersion corrections in this work. Note the dominant intrinsic defects of $MAPbI_3$ do not induce any deep charge-state transition energy levels in the bandgap, and hence cannot act as the charged recombination centers. In particular, for V_I that has commonly been assumed to be the deep-level defect[19], our calculation suggests V_I behaves only +1 charged state over the whole range of Fermi energy with the transition level $\varepsilon(+1/-1)$ slightly above the conduction band minimum (CBM). It can be seen that V_I^+ and V_{Pb}^{2-} serves as the most stable donor and acceptor defects, regardless of the materials of the growth conditions, which therefore largely determines the charge neutrality of the material. The Fermi level is pinned approximately at the cross point between the formation energies (indicated by the vertical grey line in **Figures 2a-c**).

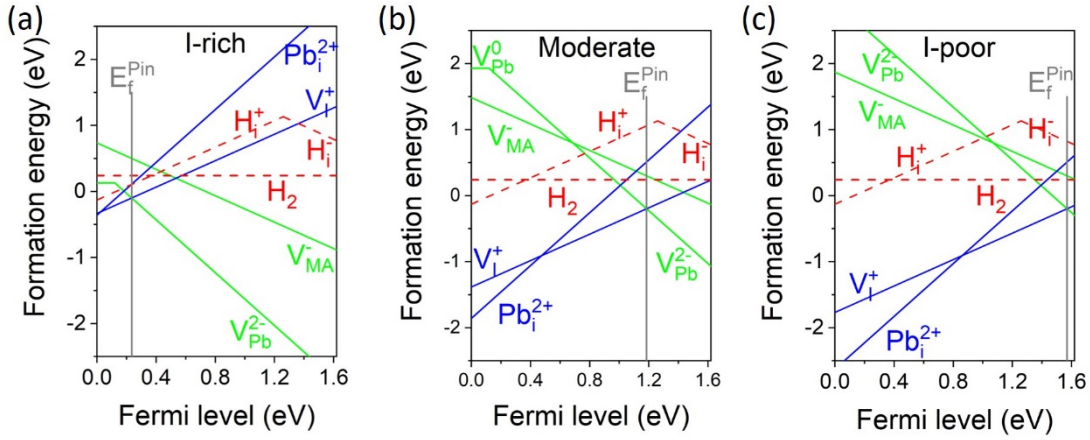

Figure 2. Formation energies of the energetically favorable intrinsic defects (V_I, Pb_i, V_{Pb}, and V_{MA}) and hydrogen interstitials (H_i and H_2) in $MAPbI_3$ as functional of Fermi level, calculated with the chemical potentials corresponding to points A (a), B (b), and C (c) in **Figure 1a**.

Under *I*-rich conditions, as shown in **Figure 2a**, the E_f is pinned at 0.23 eV above the valence band maximum (VBM), indicating that $MAPbI_3$ perovskites are *p*-type, in which H_i^+ (interstitial proton) acts as the dominant hydrogen defect. When going into

the moderate and I-poor growth conditions, as shown in **Figures 2b & 2c**, the pinned Fermi levels of the system are shifted to higher in the bandgap, located at 0.43 eV and 0.05 eV below the CBM, corresponding to intrinsic and *n*-type material properties, respectively. Electric-inactive H_2 is the dominant hydrogen interstitial under the intrinsic and *n*-type conditions. Significantly, the negatively charged monoatomic hydrogen interstitial, H_i^-, can be also formed in the perovskite layer under I-poor conditions, where the defect formation energy of 0.71 eV is quite comparable to 0.72 eV of $V_{H(N)}^-$[23], which has been known as an efficient, non-radiative recombination center for $MAPbI_3$ solar cells.

Compared with electrically inactive molecular H_2 located in the largest lattice void region, atomic, H_i has distinct position preferences depending on its charge state, i.e., H_i^+ is bonded to I anions and H_i^- is bonded to Pb cations[33] (**Figure 1b**). In particular, the incorporation of H_i^- is accompanied by a significant lattice relaxation off the lattice site, with a distinctly different local structure to H_i^+ (**Figure 1c**). Similar to the six-fold coordinated PbI_6 octahedron, with an average bond length of 3.14 Å in pure $MAPbI_3$ (**Figure 1b**), for H_i^+, the local structure of C1 is still six-fold coordinated, though the $Pb-I$ bonds near H_i^+ are slightly relaxed with the average bond length of 3.22 Å. In contrast, the H_i^- anion causes the central Pb cation to be highly distorted, moving toward the MA cation, and therefore, the local structure of PbI_6 octahedron converts from six-fold coordination to three-fold coordination by breaking three $Pb-I$ bonds. Significantly, the electronic band edges of $MAPbI_3$ perovskite are predominantly controlled by the inorganic framework of the PbI_6 octahedron: the VBM has contributions from the antibonding hybridization of the 5p orbitals of I anions and the 6s orbitals of Pb cations, the CBM is mainly composed of 6p orbits of Pb cations **(Figure S1**). Hence, the strong atomic displacement of the local PbI_6 octahedron is expected to significantly change the electronic structure around the bandgap and affect the original optoelectronic properties. Indeed, the defects involving strong local atomic displacements have been found in many technologically significant semiconductor materials, especially for hybrid perovskites due to the nature of the low energy cost for bond breaking and distortion[18,19,35]; importantly, these defects can induce deep energy levels inside the bandgap with localized wavefunctions. Consequently, the electron-hole recombination is expected to be extremely sensitive to the charge states of these defect centers.

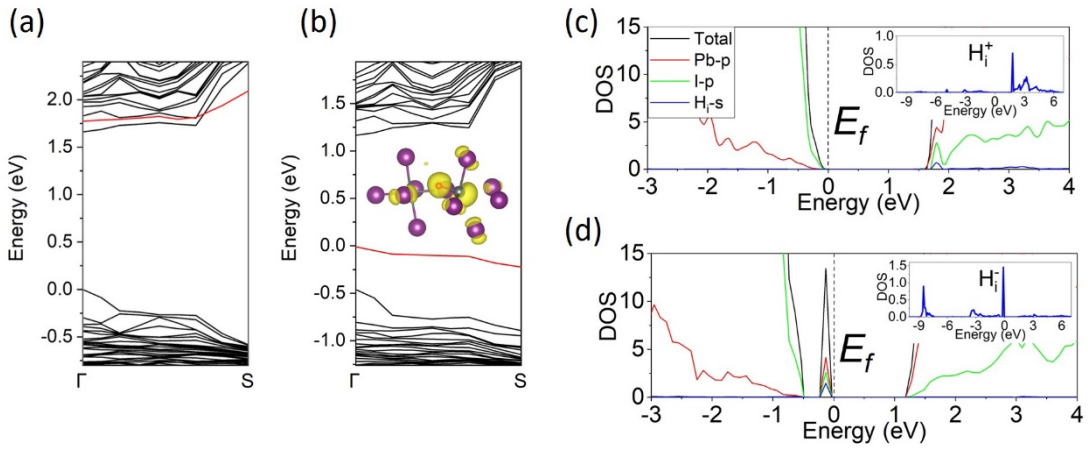

Figure 3. Band structures of $MAPbI_3$ with (a) H_i^+ in C1 and (b) H_i^- in C2 (cf. **Figure 1c**) from Γ to S $(-\frac{1}{2},\frac{1}{2},0)$, in which the inset shows the relaxed local configuration of H_i^- and the corresponding charge localization of the deep defect state. The defect orbitals are shown by red lines. Density of states of $MAPbI_3$ with (c) H_i^+ and (d) H_i^-. Fermi levels are denoted as dashed lines. The insets of (c) and (d) show the partial density of states (PDOS) of the hydrogen interstitials, respectively.

As shown in **Figure 3a**, the positively charged H_i^+ with an electronic configuration $1s^0$ does not induce any defect levels in the bandgap, but an unoccupied, conduction-band-like state slightly above the CBM. **Figure 3c** indicates that such a state is a hybridization between the Pb-6p, I-5p, and H-1s orbitals. Electrons occupying this resonance will essentially relax to the CBM, indicative of a shallow donor defect, which plays a beneficial role by producing free electron carriers. In contrast, the formation of negatively charged H_i^- with an electronic configuration $1s^2$ leads to the creation of a deep fully occupied level lying in the bandgap, as shown in **Figure 3b**. This deep-defect level is located at around 0.45 eV above the VBM; notice the yellow sphere contour plot of the orbital wavefunction around H, Pb, and I, in the inset of **Figure 3b**. Therefore, such a gap state is mainly composed of I-5p, Pb-6p, and H-1s states, as shown by the density of states in **Figure 3d**. Interestingly, photoconductivity measurements recorded a deep trap state at around 459 meV for the electron carriers in $MAPbI_3$ perovskite films synthesized under I-poor conditions[36], in a vacuum chamber

excluding most external impurities. A careful inspection of band structures and wave functions indicates that no intrinsic defect levels are induced at around 0.45 eV above the VBM. The deprotonation of MA cations is a robust intrinsic source for generating interstitial hydrogen within the lattice[29]. It is plausible that such a deep trap state lying in the bandgap could come from H_i^-. H_i^- is an efficient channel for electron-hole recombination and reduces the electron-hole diffusion length and limits the open-circuit voltage (V_{OC}) in the solar cells. Therefore, H_i^- is highly detrimental to the perovskite photovoltaic performance and should be minimized.

One strategy to minimize H_i^- is to optimize the growth conditions for the perovskite layer. From **Figure 2**, I-poor growth conditions favor n-type MAPbI3, where the formation of H_i^- is energetically favorable, in addition to the previously reported detrimental $V_{H(N)}^-$[23]. Both deep-level H_i^- (abundant under hydrogen-rich conditions) and $V_{H(N)}^-$ (abundant under hydrogen-poor conditions) have deleterious effects on free carrier transport, which is in good agreement with the experimental fact that synthesizing the materials with iodide-poor conditions reduces the solar cell efficiencies[11]. In contrast, I-rich conditions favor p-type materials and hence prevent the formation of H_i^- and $V_{H(N)}^-$. However, it also promotes the formation of intrinsic iodine interstitials, I_i, which can also induce carrier recombination[21], and hence leads to a drop in perovskite solar cell efficiencies. Therefore, delicate control of I environment for the perovskite layers is key to enabling the device with improved efficiencies; the moderate growth conditions could mitigate the concentrations of these unfavorable defects to minimize the impact of recombination, which is supported by experimental results[11,37].

On the other hand, extrinsic doping could be a viable approach to modulate the defect property via changing the local atomic configuration around the defect center; for instance, Zn doping in p-type CdTe enhances the lattice strain to prevent the atomic relaxation to the detrimental AX configuration of the deep level[38]. The formation of the deep localized state of H_i^- in $MAPbI_3$ is accompanied by the formation of three-fold coordinated PbI_6 by breaking three $Pb-I$ bonds, as seen in the case of the three-fold coordinated DY center in Bi-doped $MAPbBr_3$[35], where a deep localized state is generated in the bandgap. Generally, in halide perovskites, the $Br-Pb$ bond is stronger than the $I-Pb$ bond[39], because Br has a higher electronegativity than I.

Therefore, Br-doping is expected to prevent the significant atomic displacement around the defect site and passivate the detrimental deep-level of H_i^-.

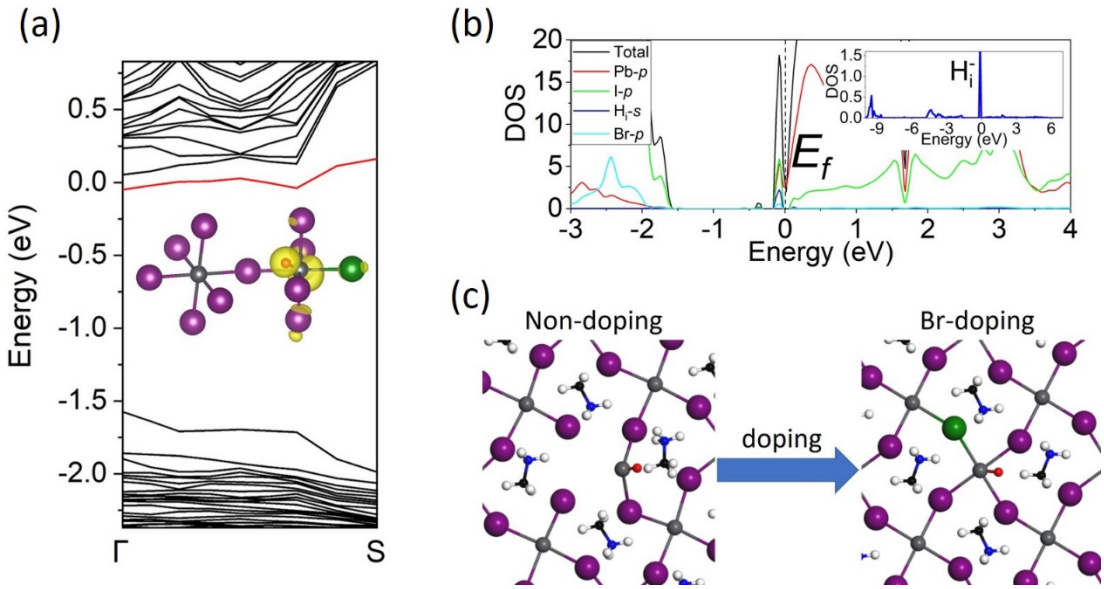

Figure 4. (a) Band structure of Br-doped $MAPbI_3$ with H_i^- from Γ to S $(-\frac{1}{2},\frac{1}{2},0)$. The inset shows the relaxed local atomic configuration and the corresponding charge localization of the defect state, shown by the red line. (b) DOS of Br-doped $MAPbI_3$ with H_i^-. The inset shows the PDOS of the hydrogen anion. (c) Schematic illustration of the mechanism of Br-passivation of detrimental H_i^- in $MAPbI_3$. The Br atom is depicted as a green sphere and other notations are as those in **Figure 1**.

To assess the effect of Br-doping in $MAPbI_3$, we substituted each of the six I atoms of the local PbI_6 octahedra around H_i^- by one Br atom, as shown in **Figure S2a**. The energetically most stable configuration is shown in **Figure 4c**. We further calculated the energetics for the substitutional Br_I far from the H_i^- site (**Figure S2b**) for comparison. The **Figure 4c** configuration is more stable than the **Figure S2b** configuration by 0.63 eV, indicating Br atoms reside energetically favorably around H_i^- during doping. Significantly, it was found that Br has a strong driving force to restore Pb back to its original atomic location, due to the stronger $Pb-Br$ bond. Therefore, the local three-fold coordinated inorganic framework effectively transforms back to the original six-fold coordinated octahedra. The bond length of $Pb-Br$, 2.87

Å, is slightly shorter than the average length of $Pb-I$ bonds, which agrees with the measured smaller lattice constant of $MAPbBr_3$ compared to $MAPbI_3$ from both experiments[40] and theoretical calculations[41]. It can be seen that, along with local symmetry changing from three-fold coordination to six-fold coordination, the deep-localized state of H_i^- moves up and becomes a shallow state, as shown in **Figures 4a and 4b**. The shallow level is fully occupied, and the occupied electrons can easily hop into the CBM, playing the role of donating free electrons for the perovskite. Moreover, note such a conduction-band-like level near the bottom of the conduction band can play a similar role as the CBM with accepting the photo-excited electrons as the free carriers for the conduction band, hence, reducing the bandgap of the host perovskites in principle. The calculated bandgap after Br doping of 1.53 eV is closer to the optimum value represented by the Shockley-Queisser Limit (~1.3 eV)[17]. These results demonstrate how Br mixing can effectively passivate the detrimental effect of deep-level H_i^-, and explain the experimental findings that light Br doping is beneficial for achieving a superior efficiency for $MAPbI_3$ perovskite solar cells[42].

Conclusions

In summary, based on DFT calculations, we have examined the formation and distinct roles of the interstitial hydrogen defects in the efficiency of the perovskite solar cells, and in particular, revealed the highly detrimental cause of electron-hole recombination behavior by H_i^-. We found that, under I-poor growth conditions, H_i^- can be incorporated in $MAPbI_3$ accompanied by large atomic displacements around the defect site, resulting in distinctly different properties to H_i^+, which is a shallow donor. H_i^- creates a deep localized trapping state as an efficient recombination center for free carriers, detrimental to the solar cell performance. Our study suggested that controlling the growth conditions of the material can help to minimize such recombination centers; this indeed agrees with the empirical experience in $MAPbI_3$ and the careful control of the I concentration during synthesis. Alternatively, the appropriate addition of Br can also drastically passivate the recombination process by reducing the gap state via changing the defect local configuration, which gives a microscopic explanation for the exceptionally improved efficiencies of Br-doped perovskite solar cells.

Computational Method

First-principles calculations were performed using density functional theory (DFT)[43] as implemented in Vienna Ab initio Simulation Package (VASP) code[44]. Projector augmented wave (PAW) pseudopotentials were used to model the valence states and the interactions between core and valence electrons[45]. The generalized gradient approximation (GGA) parameterized by Perdew, Burke, and Ernzerhof (PBE) was employed as the exchange-correlation functional[46]. The Tkatchenko-Scheffler (TS) scheme[47] was used for describing the dispersion interactions for the hybrid perovskite systems[48]. The kinetic energy cutoff of the plane-wave basis was set at 400 eV. Experimentally, $MAPbI_3$ has an orthorhombic (Pnma) crystal structure[49]. For defect calculations, a $3 \times 3 \times 1$ 432-atom supercell with a Monkhorst–Pack sampling of $2 \times 2 \times 2$ k-points was employed. All atoms were fully relaxed until the forces on atoms are less than 0.01 eV/Å. Our PBE calculated bandgap (1.51 eV) is slightly underestimated for $MAPbI_3$, compared with the experimental value of 1.61 eV[50]. The more accurate Heyd–Scuseria–Ernzerhof hybrid functional with the spin-orbit coupling (HSE-SOC) method gives a bandgap value of 1.62 eV. Therefore, the defect calculations were conducted at HSE-SOC-TS level. We further performed the convergence test based on $3 \times 2 \times 2$ 576-atom supercell, focusing on charged H_i^+ and H_i^-, of which the calculated formation energy differences are only xxx and xxx eV, respectively.

The calculation of defect formation energy follows the established method[51], which is defined as the equation below:

$$\Delta H_f\left(H_i^q\right) = E\left(H_i^q\right) - E(host) - \sum n_i(\mu_i + \Delta\mu_i) + q(E_f + E(VBM) + \Delta V) \qquad (1)$$

where $E\left(H_i^q\right)$ and $E(host)$ are total energies with and without defect, respectively. n_i indicates the number of defects added into the supercell. μ_i is the absolute value of the chemical potential of the defect atoms; for the case of hydrogen, it is given by half of the total energy of the H_2 molecule. $\Delta\mu_i$ stands for the relative value of the chemical potential, which is related to growth conditions. The Fermi energy, E_f, is referenced to the VBM of $MAPbI_3$, and $E(VBM)$ represents the energy of VBM. ΔV is added for correcting the effect of periodic images of charged defects[52]. The transition level is defined as the Fermi-level position with respect to the bulk VBM for which the formation energies of different defect charge states are equal, thus, can be determined

by:

$$\mathcal{E}(q/q') = [E(a,q) - E(a,q') - (q-q')(E(VBM) + \Delta V)]/(q-q') \quad (2)$$

When the single-phase $MAPbI_3$ is stable with respect to the secondary phases of MAI and PbI_2, the chemical potential of the host should satisfy the conditions:

$$\Delta\mu_{MA} + \Delta\mu_{Pb} + 3\Delta\mu_I = \Delta H_f(MAPbI_3)$$

$$\Delta\mu_{MA} + \Delta\mu_I < \Delta H_f(MAI)$$

$$\Delta\mu_{Pb} + 2\Delta\mu_I < \Delta H_f(PbI_2)$$

where $\Delta H_f(MAPbI_3)$, $\Delta H_f(MAI)$, and $\Delta H_f(PbI_2)$ are the formation enthalpies of $MAPbI_3$, MAI, and PbI_2, respectively. To avoid the formation of elemental phases, all the chemical potentials should be less than zero ($\Delta\mu_{MA} < 0$, $\Delta\mu_{Pb} < 0$, and $\Delta\mu_I < 0$).

Acknowledgements

We acknowledge the expert support provided by the Sydney Informatics Hub (SIH) team—a core research facility of the University of Sydney. This work was supported by computational resources provided by the Australian Government through Gadi under the National Computational Merit Allocation Scheme and was accessed through the SIH HPC Allocation Scheme [LE190100021]. We acknowledges partial financial support from the Australian Research Council [DP200100940] and [DE180100167].

Conflict of Interest

The authors declare no conflict of interest.

References

1 *Nat. Energy*, 2019, **4**, 1–1.

2 W. Hui, L. Chao, H. Lu, F. Xia, Q. Wei, Z. Su, T. Niu, L. Tao, B. Du, D. Li, Y. Wang, H. Dong, S. Zuo, B. Li, W. Shi, X. Ran, P. Li, H. Zhang, Z. Wu, C. Ran, L. Song, G. Xing, X. Gao, J. Zhang, Y. Xia, Y. Chen and W. Huang, *Science*, 2021, **371**, 1359–1364.

3 Y. Liang, F. Li and R. Zheng, *Advanced Electronic Materials*, 2020, **6**, 2000137.
4 L. N. Quan, B. P. Rand, R. H. Friend, S. G. Mhaisalkar, T.-W. Lee and E. H. Sargent, *Chem. Rev.*, 2019, **119**, 7444–7477.
5 Y. Hassan, J. H. Park, M. L. Crawford, A. Sadhanala, J. Lee, J. C. Sadighian, E. Mosconi, R. Shivanna, E. Radicchi, M. Jeong, C. Yang, H. Choi, S. H. Park, M. H. Song, F. De Angelis, C. Y. Wong, R. H. Friend, B. R. Lee and H. J. Snaith, *Nature*, 2021, **591**, 72–77.
6 G. Xing, N. Mathews, S. Sun, S. S. Lim, Y. M. Lam, M. Grätzel, S. Mhaisalkar and T. C. Sum, *Science*, 2013, **342**, 344–347.
7 N. Wang, W. Liu and Q. Zhang, *Small Methods*, 2018, **2**, 1700380.
8 M. M. Lee, J. Teuscher, T. Miyasaka, T. N. Murakami and H. J. Snaith, *Science*, 2012, **338**, 643–647.
9 A. Kojima, K. Teshima, Y. Shirai and T. Miyasaka, *J. Am. Chem. Soc.*, 2009, **131**, 6050–6051.
10 Best Research-Cell Efficiency Chart, https://www.nrel.gov/pv/assets/pdfs/best-research-cell-efficiencies.20200104.pdf, (accessed July 5, 2021).
11 W. S. Yang, B.-W. Park, E. H. Jung, N. J. Jeon, Y. C. Kim, D. U. Lee, S. S. Shin, J. Seo, E. K. Kim, J. H. Noh and S. I. Seok, *Science*, 2017, **356**, 1376–1379.
12 Y. Zhou, I. Poli, D. Meggiolaro, F. De Angelis and A. Petrozza, *Nat. Rev. Mater.*, 2021, 1–17.
13 D. Luo, R. Su, W. Zhang, Q. Gong and R. Zhu, *Nat. Rev. Mater.*, 2020, **5**, 44–60.
14 N. J. Jeon, J. H. Noh, W. S. Yang, Y. C. Kim, S. Ryu, J. Seo and S. I. Seok, *Nature*, 2015, **517**, 476–480.
15 F. Ye, J. Ma, C. Chen, H. Wang, Y. Xu, S. Zhang, T. Wang, C. Tao and G. Fang, *Adv. Mater.*, 2021, **33**, 2007126.
16 F. Zhang, B. Yang, X. Mao, R. Yang, L. Jiang, Y. Li, J. Xiong, Y. Yang, R. He, W. Deng and K. Han, *ACS Appl. Mater. Interfaces*, 2017, **9**, 14827–14832.
17 W. Shockley and H. J. Queisser, *J. Appl. Phys.*, 1961, **32**, 510–519.
18 J. Wang, W. Li and W. Yin, *Adv. Mater.*, 2020, **32**, 1906115.
19 M. L. Agiorgousis, Y.-Y. Sun, H. Zeng and S. Zhang, *J. Am. Chem. Soc.*, 2014, **136**, 14570–14575.
20 S. Heo, G. Seo, Y. Lee, D. Lee, M. Seol, J. Lee, J.-B. Park, K. Kim, D.-J. Yun, Y. S. Kim, J. K. Shin, T. K. Ahn and M. K. Nazeeruddin, *Energy Environ. Sci.*, 2017, **10**, 1128–1133.
21 X. Zhang, M. E. Turiansky, J.-X. Shen and C. G. Van de Walle, *Phys. Rev. B*, 2020, **101**, 140101.
22 D. Meggiolaro and F. De Angelis, *ACS Energy Lett.*, 2018, **3**, 2206–2222.
23 X. Zhang, J.-X. Shen, M. E. Turiansky and C. G. Van de Walle, *Nat. Mater.*, 2021, **20**, 971–976.
24 D. R. Ceratti, A. Zohar, R. Kozlov, H. Dong, G. Uraltsev, O. Girshevitz, I. Pinkas, L. Avram, G. Hodes and D. Cahen, *Advanced Materials*, 2020, **32**, 2002467.
25 C. Cardenas-Daw, T. Simon, J. K. Stolarczyk and J. Feldmann, *J. Am. Chem. Soc.*, 2017, **139**, 16462–16465.
26 S. Sadhu, T. Buffeteau, S. Sandrez, L. Hirsch and D. M. Bassani, *J. Am. Chem. Soc.*, 2020, **142**, 10431–10437.
27 Y. Feng, Y. Zhao, W.-K. Zhou, Q. Li, W. A. Saidi, Q. Zhao and X.-Z. Li, *J. Phys. Chem. Lett.*, 2018, **9**, 6536–6543.
28 Y.-F. Chen, Y.-T. Tsai, L. Hirsch and D. M. Bassani, *J. Am. Chem. Soc.*, 2017, **139**, 16359–16364.
29 J. M. Frost and A. Walsh, *Acc. Chem. Res.*, 2016, **49**, 528–535.

30 N. Ahn, K. Kwak, M. S. Jang, H. Yoon, B. Y. Lee, J.-K. Lee, P. V. Pikhitsa, J. Byun and M. Choi, *Nat. Commun.*, 2016, **7**, 13422.
31 A. A. Said, J. Xie and Q. Zhang, *Small*, 2019, **15**, 1900854.
32 P. Delugas, A. Filippetti and A. Mattoni, *Phys. Rev. B*, 2015, **92**, 045301.
33 Y. Liang, X. Cui, F. Li, C. Stampfl, S. P. Ringer and R. Zheng, *CHEM MATER*.
34 W.-J. Yin, T. Shi and Y. Yan, *Appl. Phys. Lett.*, 2014, **104**, 063903.
35 J.-L. Li, J. Yang, T. Wu and S.-H. Wei, *J. Mater. Chem. C*, 2019, **7**, 4230–4234.
36 G. Gordillo, C. A. Otálora and A. A. Ramirez, *Phys. Chem. Chem. Phys.*, 2016, **18**, 32862–32867.
37 D.-Y. Son, J.-W. Lee, Y. J. Choi, I.-H. Jang, S. Lee, P. J. Yoo, H. Shin, N. Ahn, M. Choi, D. Kim and N.-G. Park, *Nat. Energy*, 2016, **1**, 1–8.
38 J.-H. Yang, W.-J. Yin, J.-S. Park, J. Ma and S.-H. Wei, *Semicond. Sci. Technol.*, 2016, **31**, 083002.
39 K. Li, L.-Y. Dong, H.-X. Xu, Y. Qin, Z.-G. Li, M. Azeem, W. Li and X.-H. Bu, *Mater. Chem. Front.*, 2019, **3**, 1678–1685.
40 P. Pistor, T. Burwig, C. Brzuska, B. Weber and W. Fränzel, *J. Mater. Chem. A*, 2018, **6**, 11496–11506.
41 E. Mosconi, P. Umari and F. D. Angelis, *Phys. Chem. Chem. Phys.*, 2016, **18**, 27158–27164.
42 S. Mahesh, J. M. Ball, R. D. J. Oliver, D. P. McMeekin, P. K. Nayak, M. B. Johnston and H. J. Snaith, *Energy Environ. Sci.*, 2020, **13**, 258–267.
43 W. Kohn and L. J. Sham, *Phys. Rev.*, 1965, **140**, A1133–A1138.
44 G. Kresse and J. Furthmüller, *Comput. Mater. Sci.*, 1996, **6**, 15–50.
45 G. Kresse and D. Joubert, *Phys. Rev. B*, 1999, **59**, 1758–1775.
46 J. P. Perdew, K. Burke and M. Ernzerhof, *Phys. Rev. Lett.*, 1996, **77**, 3865–3868.
47 A. Tkatchenko and M. Scheffler, *Phys. Rev. Lett.*, 2009, **102**, 073005.
48 C. Motta, F. El-Mellouhi, S. Kais, N. Tabet, F. Alharbi and S. Sanvito, *Nat. Commun.*, 2015, **6**, 7026.
49 M. T. Weller, O. J. Weber, P. F. Henry, A. M. Di Pumpo and T. C. Hansen, *Chem. Commun.*, 2015, **51**, 4180–4183.
50 Y. Yamada, T. Nakamura, M. Endo, A. Wakamiya and Y. Kanemitsu, *Appl. Phys. Express*, 2014, **7**, 032302.
51 S.-H. Wei, *Comput. Mater. Sci.*, 2004, **30**, 337–348.
52 S. Lany and A. Zunger, *Phys. Rev. B*, 2008, **78**, 235104.

Table of Contents

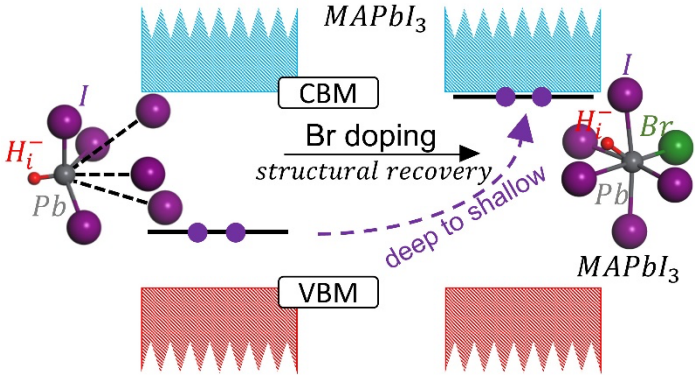

Comprehensive first-principles defect studies uncover that the hydrogen anions (H_i^-) are a new and highly detrimental cause of charge carrier recombination losses in the $MAPbI_3$ perovskite solar cells. Iodine-poor growth conditions mitigate the formation of H_i^-. Moreover, Br doping prevents the large atomic displacement caused by the presence of hydrogen anion interstitials, and hence effectively suppresses the formation of the deep localized states that act as the recombination centers.